Korean J. Chem. Eng., 36(4), 522-528 (2019)
DOI: 10.1007/s11814-019-0239-5

pISSN: 0256-1115
eISSN: 1975-7220

Structural properties of disordered macroporous $La_2O_2CO_3$/ZnO materials prepared by a solution combusion method

Hongyan Yu*,, Yong Men**, and Eun Woo Shin*,†**

*School of Chemical Engineering, University of Ulsan, Daehakro 93, Nam-gu, Ulsan 44610, Korea
**College of Chemistry and Chemical Engineering, Shanghai University of Engineering Science, No. 333 Longteng Road, Songjiang District, Shanghai 201620, P. R. China
(*Received 23 November 2018 • accepted 30 January 2019*)

Abstract−Disordered macroporous $La_2O_2CO_3$/ZnO materials were prepared by a solution combustion method, and then their microstructures and $La_2O_2CO_3$ phases were investigated as functions of La/Zn ratios and calcination temperatures. All of the materials prepared by the solution combustion method clearly showed disordered macroporous morphology whose framework was composed of ZnO and $La_2O_2CO_3$ nanoparticles. A monoclinic $La_2O_2CO_3$ structure was mainly formed in the disordered macroporous materials at La/Zn=1 and 2. In contrast, the conventional co-precipitation of $La_2O_2CO_3$/ZnO materials dominantly formed a hexagonal $La_2O_2CO_3$ phase with aggregating morphology of ZnO and $La_2O_2CO_3$ nanoparticles. However, nanocrystalline sizes of ZnO (7-10 nm) and monoclinic $La_2O_2CO_3$ (12-14 nm) in the disordered macroporous structure were much smaller than those (29-36 nm for ZnO and 44-58 nm for hexagonal $La_2O_2CO_3$) by conventional co-precipitation. In addition, the high temperature calcination at 700 °C increased the ZnO nanocrystallite size (24 nm) in the disordered macroporous framework, with transforming $La_2O_2CO_3$ into La_2O_3. This result implies that the interaction between monoclinic $La_2O_2CO_3$ and ZnO in the disordered macroporous structure inhibited ZnO nanoparticle agglomeration.

Keywords: $La_2O_2CO_3$ Phases, Disordered Macroporosity, Solution Combustion, Nanoparticle Sizes, Structural Properties

INTRODUCTION

Lanthanum has been widely employed as an electronic material [1], a special glass for optical devices [2], and in catalysts (or supports) [3-6] because it has unique electric, optical, and catalytic properties due to its partially filled 4f shell electronic configuration. The solid state compounds of lanthanum have also been used for diverse applications in the forms of oxide, hydroxide, carbonate, titanate and oxycarbonate [7-14]. Specially, lanthanum oxycarbonate has been reported as a promising CO_2 sensor and efficient catalyst (or support). Single phase $La_2O_2CO_3$ nanoparticles were synthesized by a hydrothermal process, resulting in good sensing properties for CO_2 [8]. The $La_2O_2CO_3$ phase was also introduced as a catalyst support for hydrogen production processes and an active intermediate of La_2O_3 in the dry reforming of methane [9,11]. Recently, $La_2O_2CO_3$/ZnO materials were used as catalysts for CO_2-based reactions [12-14] and as commercially-available heterogeneous catalysts for microwave-assisted biofuel production [15].

Controlling the structural properties (including size, shape, and phase) is of considerable interest because it is a key variable influencing material performance [8,10-12,16-18]. The size of $La_2O_2CO_3$ nanoparticles had an effect on the catalytic activity and CO_2-sensing response [8,16]. Porous $La_2O_2CO_3$ material made of hollow microspheres was successfully fabricated and applied for fluorescent biological labeling [17]. Metal catalysts supported by nanorod-shaped $La_2O_2CO_3$ exhibited excellent catalytic performance in selective hydrogenation and dry reforming of methane [10,11]. The existence of $La_2O_2CO_3$ phase in the dry reforming of methane enhanced the removal of carbonaceous deposits from neighboring active sites [11,19,20].

Meanwhile, ordered or disordered macroporous La-containing materials have been prepared by various methods [12,21,22]. Sadakane et al. introduced a facile preparation route to form ordered-macroporous perovskite-type mixed $La_{1-x}Sr_xFeO_3$ materials using colloidal crystal templating method [21]. Disordered macroporous $La_{1-x}K_xCo_{1-y}Fe_yO_3$ complex oxide catalysts were synthesized by an ethylene glycol-ligation and solution combustion method and used for diesel soot combustion [22]. In addition, the disordered macroporous $La_2O_2CO_3$/ZnO materials were prepared by a solution combustion method [12]. The $La_2O_2CO_3$ phase influenced the catalytic performance in studies of $La_2O_2CO_3$/ZnO materials for glycerol carbonylation with CO_2; the monoclinic $La_2O_2CO_3$ phase in the materials was superior to the hexagonal $La_2O_2CO_3$ phase in the production of glycerol carbonate [12]. However, in literature, the structural properties of the disordered macroporous $La_2O_2CO_3$/ZnO materials have not yet been investigated in detail.

In this study, disordered macroporous $La_2O_2CO_3$/ZnO materials were prepared by a solution combustion method, and their microstructures and phases were investigated as functions of the La/Zn ratios and the calcination temperatures to understand their structural properties. The disordered macroporous structure of the materials was well developed with the formation of monoclinic

†To whom correspondence should be addressed.
E-mail: ewshin@ulsan.ac.kr

Table 1. Physicochemical properties of $La_2O_2CO_3$/ZnO composite materials

Sample	S_{BET} (m^2/g)	Pore volume (cm^3/g)	La/Zn*	Crystallite size (nm)**		
				Hexagonal $La_2O_2CO_3$	Monoclinic $La_2O_2CO_3$	ZnO
LZ-0.125-550	28.1	0.327	0.114	-	-	7
LZ-0.25-550	36.5	0.285	0.180	-	12	4
LZ-1-550	17.4	0.128	1.373	-	14	10
LZ-2-550	14.4	0.137	1.735	8	14	10
CoLZ-0.125-500	10.8	0.117	0.095	44	20	35
CoLZ-0.25-500	10.9	0.116	0.197	58	-	36
CoLZ-1-500	10.9	0.142	1.158	58	-	35
CoLZ-2-500	38.1	0.353	2.417	58	-	29

*Values were obtained from the EDS elemental analysis
**Values were calculated using the Scherrer equation for the corresponding XRD characteristic peaks of the phases

$La_2O_2CO_3$ phase irrespective of the La/Zn ratios as well as the calcination temperatures. Even at high temperature calcination (700 °C), the disordered macroporous morphology was maintained while the monoclinic $La_2O_2CO_3$ was transformed into La_2O_3. The disordered macroporous $La_2O_2CO_3$/ZnO materials in this study have a potential as a heterogeneous catalyst for CO_2-related or heavy-coke-generated chemical reactions.

EXPERIMENTAL

1. Catalyst Preparation

We prepared disordered macroporous $La_2O_2CO_3$/ZnO materials by a solution combustion method [12]. In the preparation, $Zn(NO_3)_2{\cdot}6H_2O$ (Sigma-Aldrich Korea, Gyounggi, South Korea) and $La(NO_3)_3{\cdot}9H_2O$ (Sigma-Aldrich Korea, Gyounggi, South Korea) were used as starting materials. Two precursors were dissolved into the ethylene glycol solution at ambient temperature for 2 h. After complete mixing, moderate amounts of methanol were added. Then, the ethylene glycol-methanol solution was mixed with metal nitrates, heated in a muffle furnace with the ramping rate of 1 °C/min to the selected calcination temperature, and held there for 5 h. The final products were named as "LZ-x-y" where x and y indicate the La and Zn atomic ratio and the calcination temperature, respectively.

For comparison, another type of $La_2O_2CO_3$/ZnO materials was synthesized by a conventional co-precipitation method. $Zn(NO_3)_2{\cdot}6H_2O$ (Sigma-Aldrich Korea, Gyounggi, South Korea) and $La(NO_3)_3{\cdot}9H_2O$ (Sigma-Aldrich Korea, Gyounggi, South Korea) were well dissolved into a 2 M NaOH solution, and the mixed solution was added dropwise to deionized water. The detailed procedure for the preparation is described elsewhere [12]. The materials calcined at different temperatures were named as "CoLZ-x-y," where x and y indicate the La and Zn atomic ratio and the calcination temperature, respectively.

2. Catalyst Characterizations

The surface areas and pore size distributions of the catalysts were characterized by a nitrogen adsorption-desorption technique (Micromeritics ASAP 2020, Norcross, GA, USA). The samples were measured at −196 °C using an automatic analyzer. The morphologies of catalyst surfaces were observed by field-emission scanning electron microscopy (FE-SEM-EDX, JEOL, JSM-600F, Tokyo, Japan) with an energy dispersive spectrometer and a high-resolution transmission electron microscopy (TEM) instrument (JEM-2100F, JEOL, Tokyo, Japan). The X-ray diffraction (XRD) patterns were measured on a Rigaku D/MAX-2200 powder X-ray diffractometer (Rigaku Corp., Tokyo, Japan) using a Cu Kα radiation source (λ=0.15418 nm). The X-ray tube was operated at 35 kV and 20 mA, and the two theta angle was scanned from 10 to 90° (step wise 0.02°) at a speed of 2°/min. The infrared spectra of the composite materials were collected using a Nicolet 380 Fourier transform infrared (FTIR) spectrophotometer (ThermoFisher Scientific Co., Waltham, MA, USA). The spectrum was acquired by adding 124 scans with a resolution of 4 cm^{-1}.

RESULTS AND DISCUSSION

The physicochemical properties of the materials prepared by solution combustion and conventional co-precipitation methods are listed in Table 1. The Brunauer-Emmett-Teller (BET) surface areas of the LZ and CoLZ materials were in the range of 10.8-38.1 m^2/g, which is similar to those in the literature [12-14]. There was no trend in BET surface area with preparation methods or La/Zn

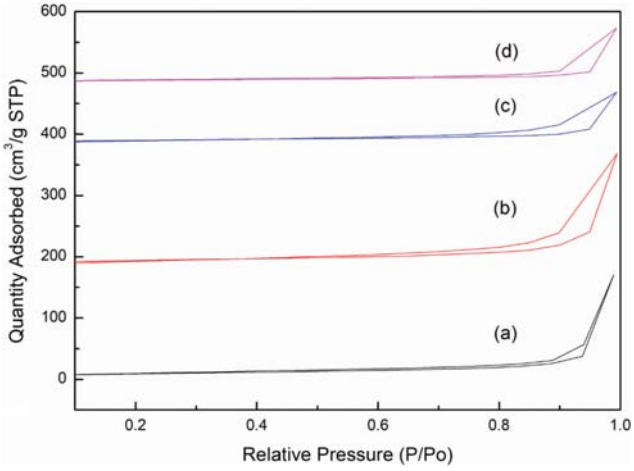

Fig. 1. Nitrogen adsorption-desorption isotherms of (a) LZ-0.125-550, (b) LZ-0.25-550, (c) LZ-1-550, and (d) LZ-2-550.

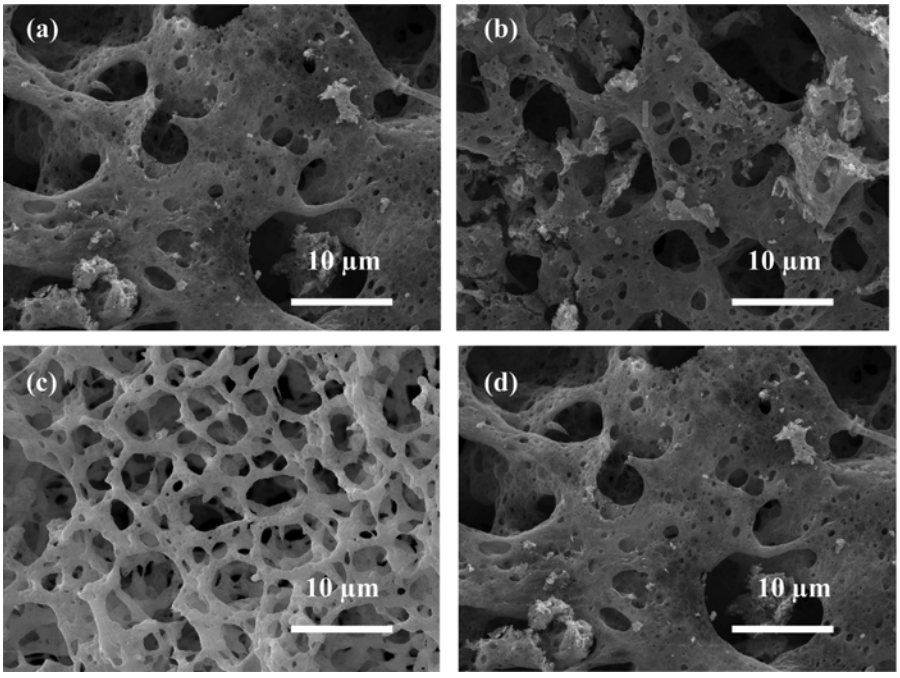

Fig. 2. FE-SEM images of (a) LZ-0.125-550, (b) LZ-0.25-550, (c) LZ-1-550, and (d) LZ-2-550.

ratio. The pore volumes also showed no trend with preparation method or La/Zn ratio (0.116-0.353 cm^3/g). Figs. 1 and S1 show the isotherms for LZ and CoLZ materials, respectively. Irrespective of the preparation methods or the existence of macropores, all of the isotherms follow the type V adsorption pattern with the type H3 hysteresis loop, implying that mesoporosity of LZ and CoLZ materials is similar. However, the values measured by the N_2 adsorption/desorption technique imply that the materials in this study were well prepared.

FE-SEM images of the LZ materials with different La/Zn ratios are displayed in Fig. 2. As a whole, all the FE-SEM images of the LZ materials clearly confirmed the disordered macroporosity generated by the solution combustion method during the preparation step. The disordered macroporosity was well developed for the LZ materials due to the release of gases in the combustion step, but there was a slight change in the disordered macroporosity depending on the La/Zn ratio. That is, the thickness of the disordered macroporous framework in the LZ materials became slightly thinner as the La/Zn ratio increased. Additionally, at La/Zn=1, the regularity of the macroporous framework (including the thickness) was relatively high (Fig. 2(c)), implying the La/Zn=1 would be an optimal value for preparing the disordered macroporous structure. Fig. S2(a)-(d) shows FE-SEM images of the CoLZ materials prepared by the conventional co-precipitation method. The CoLZ materials were composed of agglomerates of nanoparticles. As with the LZ materials, the nanoparticle morphology of the CoLZ materials changed slightly depending on the La/Zn ratio. The irregular nanoparticles with various particle sizes became larger up to a La/Zn ratio of 1. Then, the nanoparticle size in CoLZ-2-550 suddenly decreased (Fig. S2(d)). In summary, the solution combustion methods resulted in the disordered macroporosity of the LZ materials, which is clearly different from nanoparticle-aggregating morphology observed in the conventional CoLZ materials.

Meanwhile, the elemental composition in the materials was analyzed by EDS measurements. Actual La/Zn ratios are listed in Table 1 based on the results from the EDS elemental measurements. Even though the actual La/Zn values in the materials were a little different from the nominal La/Zn values, the overall trends in the La/Zn ratios were similar.

Fig. 3 shows the XRD patterns of the LZ materials prepared at various La/Zn ratios. The typical XRD characteristic peaks for zincite ZnO with a $P6_3mc$ space group (JCPDS 36-1451) were observed at 2θ=31.8°, 34.4°, 36.3°, 47.5°, 56.6°, and 62.9° for all the LZ-500

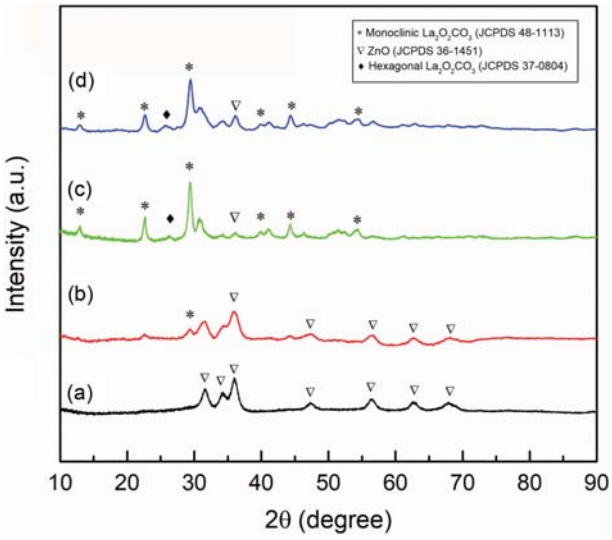

Fig. 3. XRD patterns of (a) LZ-0.125-550, (b) LZ-0.25-550, (c) LZ-1-550, and (d) LZ-2-550.

materials. The peak intensity of the ZnO phase depended on the La/Zn ratio. The XRD peak intensity of the ZnO phase decreased with increasing the La/Zn ratio, indicating the low crystallinity of the ZnO phase at high La/Zn ratios. Similarly, the ZnO crystallinity in the LZ-500 materials was relatively lower than that of the CoLZ materials when comparing the XRD peak intensities of the ZnO phase (Fig. S3). Through the Scherrer equation, the ZnO crystallite sizes for all the materials were calculated, and the values are listed in Table 1. As expected, the ZnO crystallite sizes in the LZ materials (7-10 nm) were much smaller than those in the CoLZ materials (28-36 nm), which could be related to the preparation method since the combustion method might inhibit stable growth of each nanoparticle in the LZ materials.

As shown in Fig. 3, two types of La oxycarbonate were detected: the monoclinic and hexagonal $La_2O_2CO_3$ phases. The XRD patterns of the LZ composite materials show that the monoclinic $La_2O_2CO_3$ phase was mainly observed, indicating that it was dominant in the LZ composite materials. At La/Zn=0.125, there were no XRD characteristic peaks for $La_2O_2CO_3$ phases (Fig. 3(a)). As the La/Zn ratio increased, the XRD peaks for the monoclinic $La_2O_2CO_3$ phase with a *P*63/*mmc* space group (JCPDS 48-1113) clearly appeared at 2θ=13.1°, 22.8°, 26.7°, 29.5°, and 44.4° (Fig. 3(c)). At the highest La/Zn ratio (La/Zn=2), small XRD peaks for the hexagonal $La_2O_2CO_3$ phase with a $P6_3/m$(176) space group (JCPDS 37-0804) were additionally detected (Fig. 3(d)) along with the strong existence of the monoclinic $La_2O_2CO_3$ phase. We observed the following in the LZ material series depending on the La/Zn ratios: (i) no $La_2O_2CO_3$ phases appeared at La/Zn=0.125, (ii) the monoclinic $La_2O_2CO_3$ phase was dominant at La/Zn=1 and (iii) at La/Zn=2, the monoclinic $La_2O_2CO_3$ phase was still the main $La_2O_2CO_3$ structure, whereas the hexagonal $La_2O_2CO_3$ phase existed as a shoulder. Meanwhile, the XRD patterns of the CoLZ materials showed different $La_2O_2CO_3$ phase formation behavior (Fig. S3). Monoclinic and hexagonal $La_2O_2CO_3$ phases co- existed together even at low La/Zn ratio (La/Zn=0.125) (Fig. S3(a)). As the La/Zn ratio increased, the hexagonal $La_2O_2CO_3$ phase became dominant, resulting in the formation of the highest crystalline hexagonal $La_2O_2CO_3$ phase at La/Zn=1 (Fig. S3(c)). The crystallinity of the hexagonal $La_2O_2CO_3$ phase in CoLZ-2-550 decreased a little, which was similar to the trend that the monoclinic $La_2O_2CO_3$ phase crystallinity in the LZ materials was the highest at La/Zn=1. Even in the CoLZ materials, the portion of hexagonal $La_2O_2CO_3$ phase relatively increased except for La/Zn=2. For the co-precipitation method, the hexagonal $La_2O_2CO_3$ phase was strongly formed at La/Zn=1, whereas the solution combustion method mainly generated the monoclinic $La_2O_2CO_3$ phase.

The crystallite sizes of the monoclinic and hexagonal $La_2O_2CO_3$ phases were also calculated using the Scherrer equation, and the values are listed in Table 1. The monoclinic $La_2O_2CO_3$ crystallite sizes in LZ materials increased up to 14 nm at La/Zn=1, while those in the CoLZ materials decreased from 20 nm to the point where none were formed. In contrast, the hexagonal $La_2O_2CO_3$ crystallite sizes were in the range of 44-58 nm for the CoLZ materials, clearly showing the preference for the formation of hexagonal $La_2O_2CO_3$ phase in the CoLZ series. In addition, the crystallite sizes (44-58 nm) of the hexagonal $La_2O_2CO_3$ phase in CoLZ series were much greater than those of the monoclinic $La_2O_2CO_3$ phase in LZ series (4-10 nm), implying that the growth of monoclinic $La_2O_2CO_3$ nanoparticles was suppressed in the solution combustion method.

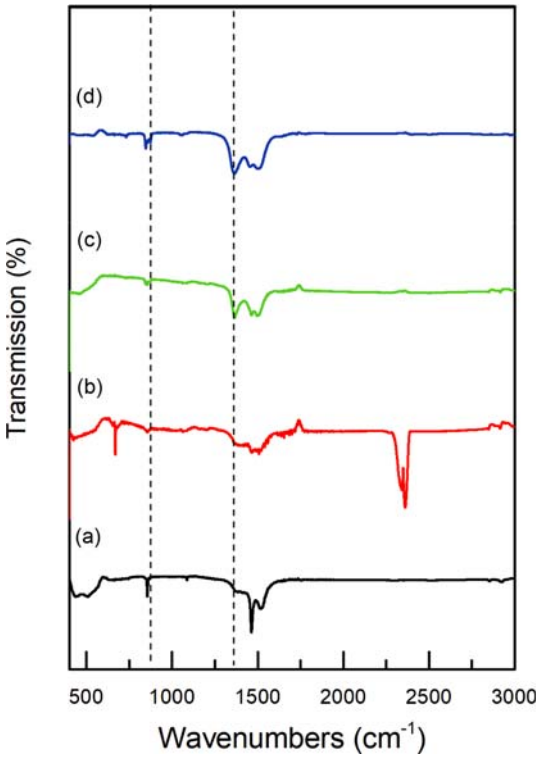

Fig. 4. FTIR spectra of (a) LZ-0.125-550, (b) LZ-0.25-550, (c) LZ-1-550, and (d) LZ-2-550.

Fig. 4 shows FTIR spectra of the LZ materials prepared at various La/Zn ratios. The assignments of typical FTIR bands for carbonates in $La_2O_2CO_3$ phases are described elsewhere in detail [23-26]. The bands at 845 cm^{-1} showed three-fold splitting due to more than one CO_3^{2-} type, and the band around 1,367 cm^{-1} was interpreted as a unique carbonate mode for the monoclinic $La_2O_2CO_3$ phase. As seen in Fig. 4, the behavior of the unique carbonate modes for the monoclinic $La_2O_2CO_3$ phase is consistent with the XRD results. The intensity of the band at 1,367 cm^{-1} apparently increased under specific conditions (La/Zn=1 or 2 of the LZ composites), matching the existence of the monoclinic $La_2O_2CO_3$ phase in the composite materials. The trend in splitting mode at 845 cm^{-1} was the same, the clear appearance of splitting bands only for the LZ materials with La/Zn=1 or 2. Therefore, FTIR spectra provided additional evidence for the preference of $La_2O_2CO_3$ phase formation in the LZ materials, which depends on the crystallinity of the $La_2O_2CO_3$ structure (La/Zn ratio) and the preparation methods.

Fig. 5 shows the TEM images for the LZ materials with different La/Zn ratios. All of the TEM images show an irregularly layered and empty-hole-like structure containing nanoparticles of *ca.* 10 nm. In contrast, dense and large nanoparticles (over 30 nm) appear in the TEM images of the CoLZ materials (Fig. S4). This is consistent with the results observed by the XRD and FE-SEM measurements.

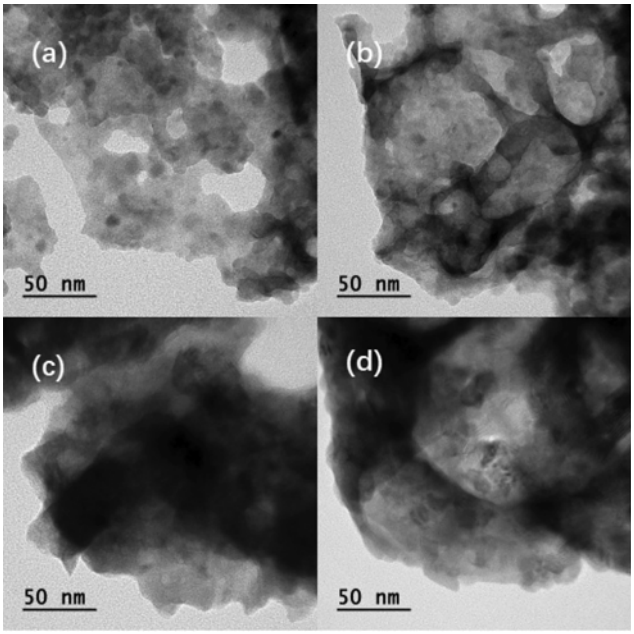

Fig. 5. HR-TEM images of (a) LZ-0.125-550, (b) LZ-0.25-550, (c) LZ-1-550, and (d) LZ-2-550.

In this study, we also investigated the structural properties of the LZ materials at different calcination temperatures. The XRD patterns of the LZ-1 composites calcined at different temperatures are shown in Fig. 6. The monoclinic $La_2O_2CO_3$ phase in the LZ-1 materials was stable up to 600 °C, but the characteristic XRD peaks for the monoclinic $La_2O_2CO_3$ phase were not detected at 650 °C and 700 °C (Fig. 6(d) and (e)). Instead, the characteristic XRD peaks for the ZnO phase became sharp and clear. At the 700 °C calcination, the characteristic XRD peaks for the La_2O_3 phase with a *P-3m1* space group (JCPDS No. 73-2141) appeared at 2θ=26.1°, 29.1°, 30.0°, 39.5°, and 46.0°, and the XRD peaks for the ZnO phase became much sharper (Fig. 6(e)). This indicates that the monoclinic $La_2O_2CO_3$ structure collapsed to La_2O_3 phase by releasing CO_2 into the gas phase, and ZnO nanoparticles agglomerated simultaneously. In contrast to this behavior, the XRD patterns of the CoLZ-1 materials remained unchanged even at 650 °C. The intensity of the characteristic XRD peaks for the hexagonal $La_2O_2CO_3$ phase was still strong irrespective of increasing calcination temperature up to 650 °C (Fig. S5), implying higher stability of the hexagonal $La_2O_2CO_3$ phase in the CoLZ-1 materials than the monoclinic $La_2O_2CO_3$ phase in the LZ-1 materials. At the 700 °C calcination, sharp characteristic XRD peaks for the La_2O_3 phase appeared instead of the peaks of the hexagonal $La_2O_2CO_3$ phase, and the peak intensity for the ZnO phase remained unchanged, which indicates transformation of the hexagonal $La_2O_2CO_3$ into the La_2O_3 phase with no agglomeration of ZnO nanoparticles.

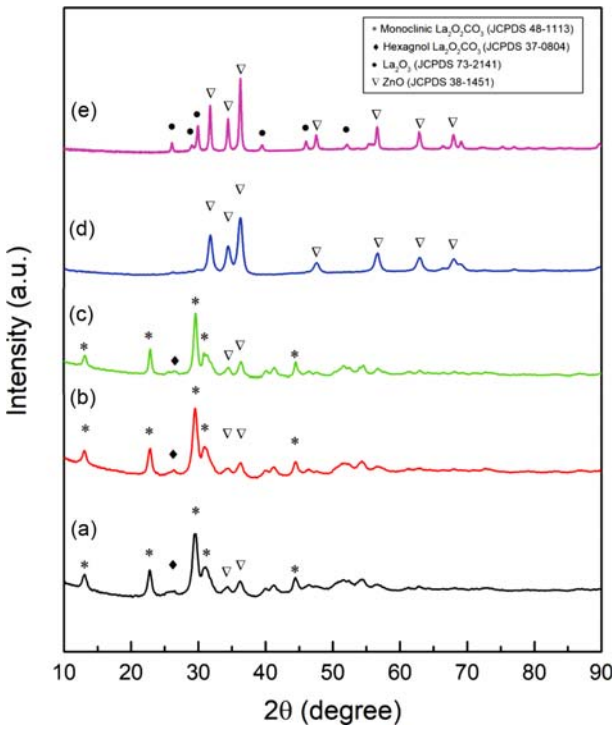

Fig. 6. XRD patterns of LZ-1 materials calcined at different temperatures. (a) T=500 °C, (b) T=550 °C, (c) T=600 °C, (d) T=650 °C, and (e) T=700 °C.

The crystallite sizes of the $La_2O_2CO_3$ and ZnO phases calcined at the different temperatures were calculated by the Scherrer equation. The values are listed in Table 2. The crystallite sizes of the $La_2O_2CO_3$ phases remained almost unchanged irrespective of increasing the calcination temperatures at around 14 nm for the LZ-1 materials and 49-58 nm for the CoLZ-1 materials. Interestingly, the behavior of ZnO crystallite sizes at various calcination temperatures depended on the preparation methods, which is clearly displayed in Fig. 7. For the CoLZ materials, the ZnO crystallite sizes were maintained at a similar value of around 34-39 nm even after the $La_2O_2CO_3$ phase was transformed into La_2O_3 phase at the 700 °C calcination. In contrast, the ZnO crystallite sizes for the LZ-1 materials suddenly increased from 10 nm to 21 and 24 nm after the CO_2 release from the monoclinic $La_2O_2CO_3$ phase at

Table 2. Crystallite sizes of each crystalline structure in LZ-1 and CoLZ-1 calcined at different temperatures

Samples	Crystallite sizes (nm)*		
	Hexagonal $La_2O_2CO_3$	Monoclinic $La_2O_2CO_3$	ZnO
LZ-1-500	-	14	13
LZ-1-550	-	14	10
LZ-1-600	-	14	10
LZ-1-650	-	-	21
LZ-1-700	-	-	24
CoLZ-1-500	58	-	35
CoLZ-1-550	49	-	34
CoLZ-1-600	58	-	39
CoLZ-1-650	54	-	38
CoLZ-1-700	-	-	39

*Values were calculated using the Scherrer equation for the corresponding XRD characteristic peaks of the phases

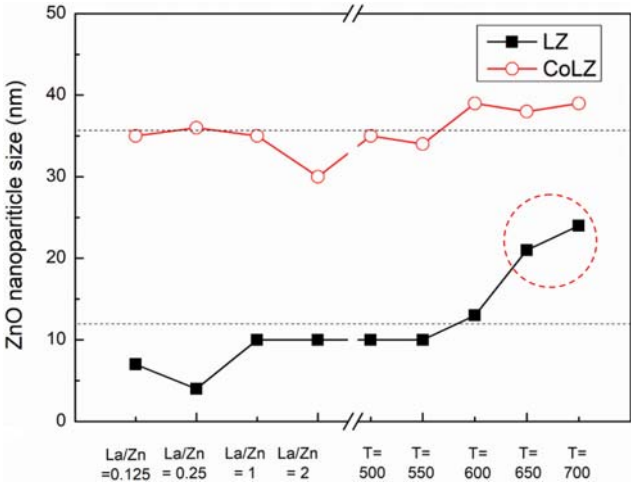

Fig. 7. ZnO nanoparticle sizes depending on the La/Zn ratios and the calcination temperatures.

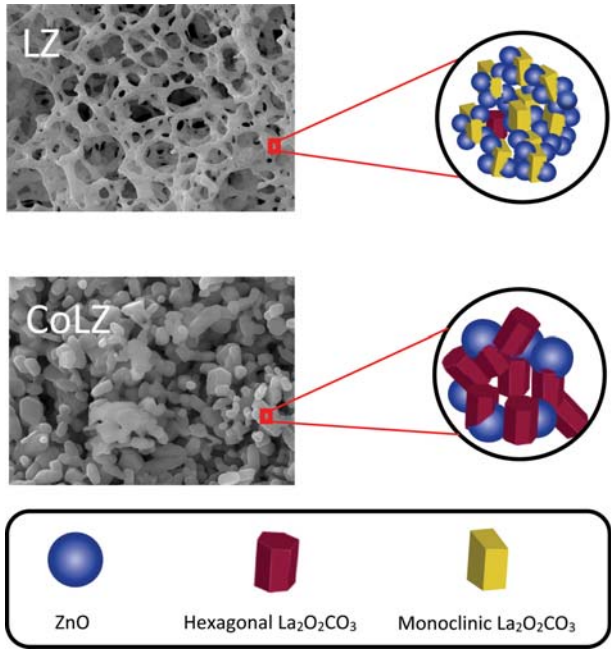

Scheme 1. Schematic illustration of morphologies and crystalline structures of LZ and CoLZ materials.

650 °C and 700 °C, respectively. Below 600 °C calcination and with different La/Zn ratios, the ZnO nanocrystalline sizes were maintained below 10 nm. Accordingly, it can be deduced that there was specific interaction between the monoclinic $La_2O_2CO_3$ phase and ZnO nanoparticles to inhibit the growth of ZnO nanoparticles in the LZ materials.

Fig. 8 shows FE-SEM images of the LZ-1 calcined at 550 °C, 650 °C and 700 °C. In spite of increasing the calcination temperature, the disordered macroporous structure in the LZ-1 composites was still maintained. However, many smaller pores were generated in the macroporous framework of the LZ-1 materials calcined at 650 °C and 700 °C (Fig. 8(b)-(c)), which is directly related to the CO_2 gas release by the phase transformation from $La_2O_2CO_3$ to La_2O_3.

A schematic illustration of the morphologies and $La_2O_2CO_3$ structures of the LZ materials is displayed in Scheme 1. In the LZ materials, the disordered macroporosity was well developed by the solution combustion method, resulting in small nanocrystallites of ZnO and monoclinic $La_2O_2CO_3$ structures. In the preparation process, ethylene glycol was oxidized to glyoxylate dianion in the solution under 100 °C due to the properties of nitrates of mixed metals. The metal glyoxylate was converted to metal oxide or metal oxycarbonate when the growing temperature reached 400 °C. Finally, $La_2O_2CO_3$ or La_2O_3 phase was clearly obtained by the calcination above 500 °C for 5 h with ZnO nanoparticles. The continuous gas release in the process of the solution combustion method not only left the disordered macroporous structure in the solid, but also induced the dominant formation of a monoclinic $La_2O_2CO_3$ phase. The presence of the monoclinic $La_2O_2CO_3$ phase in the LZ materials inhibited the growth of ZnO nanoparticles in the disordered macroporous framework due to the strong interaction between ZnO and monoclinic $La_2O_2CO_3$ nanoparticles, resulting in much smaller ZnO crystallites (4-10 nm) in the LZ materials. Conversely, the destruction of the monoclinic $La_2O_2CO_3$ phase by calcination above 650 °C caused a rapid agglomeration of ZnO nanoparticles in the LZ-1 materials (21-24 nm). On the other hand, the CoLZ materials were composed of aggregates of ZnO and hexagonal $La_2O_2CO_3$ nanoparticles. The larger crystallites of ZnO phase (29-39 nm) in the CoLZ materials indicates no interaction between hexagonal $La_2O_2CO_3$ and ZnO nanoparticles in the conventional co-precipitation process, resulting in the no difference in the ZnO crystallite sizes even after the calcination at 700 °C.

CONCLUSION

Disordered macroporous $La_2O_2CO_3$/ZnO materials were synthesized as a function of the La/Zn ratios and the calcination tem-

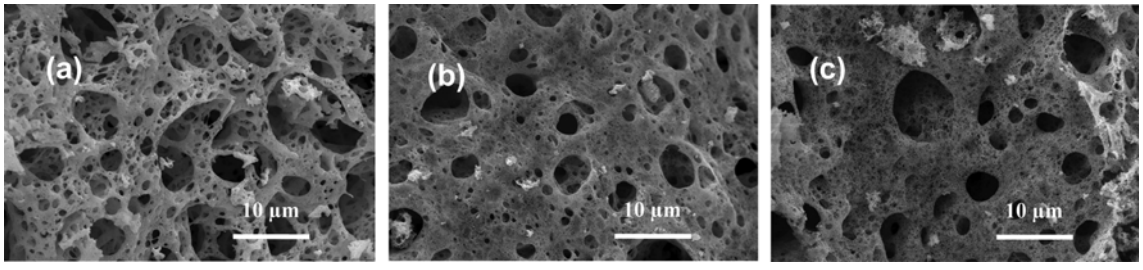

Fig. 8. FE-SEM images of LZ-1 materials calcined at different temperatures. (a) T=550 °C, (b) T=650 °C, and (c) T=700 °C.

peratures by the solution combustion method. All of the composite materials prepared by the solution combustion method clearly showed a disordered macroporous framework that was composed of ZnO and monoclinic $La_2O_2CO_3$ nanoparticles. On the contrary, the materials prepared by the conventional co-precipitation method were composed of aggregates of nanoparticles with the dominant formation of hexagonal $La_2O_2CO_3$ phase. Calcination at 700 °C transformed the $La_2O_2CO_3$ phase into La_2O_3 phase in the materials. Based on the sizes of ZnO nanoparticles, the ZnO nanoparticles in the disordered macroporous LZ composite materials interacted strongly with the monoclinic $La_2O_2CO_3$ nanoparticles, which inhibited the growth of the monoclinic $La_2O_2CO_3$ phase in the disordered macroporous LZ materials.

ACKNOWLEDGEMENTS

This research was supported by the Basic Science Research Program administered through the National Research Foundation of Korea (NRF) and funded by the Ministry of Science, and ICT (No. 2018R1A2B6004219).

SUPPORTING INFORMATION

Additional information as noted in the text. This information is available via the Internet at http://www.springer.com/chemistry/journal/11814.

REFERENCES

1. D. B. Meadowcroft, *J. Phys. D: Appl. Phys.*, **2**, 1225 (1969).
2. Q. W. Song, X. M. Wang, R. Bussjager and J. Osman, *Appl. Opt.*, **35**, 3155 (1996).
3. A. Tarjomannejad, A. Farzi, A. Niaei and D. Salari, *Korean J. Chem. Eng.*, **33**, 2628 (2016).
4. S. H. Park, B.-H. Chun and S. H. Kim, *Korean J. Chem. Eng.*, **28**, 402 (2011).
5. J. Kašpar, P. Fornasiero and N. Hickey, *Catal. Today*, **77**, 419 (2003).
6. J. Ma, M. Fang and N. T. Lau, *Appl. Catal. A Gen.*, **150**, 253 (1997).
7. G. Herrera, J. Jimenez-Mier and E. Chavira, *Mater. Charact.*, **89**, 13 (2014).
8. D. Ding, W. Lu, Y. Xiong, X. Pan, J. Zhang, C. Ling, Y. Du and Q. Xue, *Appl. Surf. Sci.*, **426**, 725 (2017).
9. L. Jia, J. Li and W. Fang, *J. Alloys Compd.*, **489**, L13 (2017).
10. F. Wang, Z. Zhang, X. Wei, Q. Fang and X. Jiang, *Appl. Catal. A Gen.*, **543**, 196 (2017).
11. X. Li, D. Li, H. Tian, L. Zeng, Z. J. Zhao and J. Gong, *Appl. Catal. B Environ.*, **202**, 683 (2017).
12. C. Park, H. Nguyen-Phu and E. W. Shin, *Mol. Catal.*, **435**, 99 (2017).
13. H. Li, D. Gao, P. Gao, F. Wang, N. Zhao, F. Xiao, W. Wei and Y. Sun, *Catal. Sci. Technol.*, **3**, 2801 (2013).
14. H. Li, X. Jiao, L. Li, N. Zhao, F. Xiao, W. Wei, Y. Sun and B. Zhang, *Catal. Sci. Technol.*, **5**, 989 (2015).
15. L. Jin, Y. Zhang, J. P. Dombrowski, C. H. Chen, A. Pravatas, L. Xu, C. Perkins and S. L. Suib, *Appl. Catal. B Environ.*, **103**, 200 (2015).
16. C. Estruch Bosch, M. P. Copley, T. Eralp, E. Bilbé, J. W. Thybaut, G. B. Marin and P. Collier, *Appl. Catal. A Gen.*, **536**, 104 (2017).
17. H. Niu, Q. Min, Z. Tao, J. Song, C. Mao, S. Zhang and Q. Chen, *J. Alloys Compd.*, **509**, 744 (2011).
18. Q. Mu and Y. Wang, *J. Alloys Compd.*, **509**, 396 (2011).
19. A. Tsoukalou, Q. Imtiaz, S. M. Kim, P. M. Abdala, S. Yoon and C. R. Müller, *J. Catal.*, **343**, 208 (2016).
20. D. Pakhare, V. Schwartz, V. Abdelsayed, D. Haynes, D. Shekhawat, J. Poston and J. Spivey, *J. Catal.*, **316**, 78 (2014).
21. M. Sadakane, T. Asanuman, J. Kubo and W. Ueda, *Chem. Mater.*, **17**, 3546 (2005).
22. G. Zhang, Z. Zhao, J. Liu, J. Xu, Y. Jing, A. Duan and G. Jiang, *J. Rare Earths*, **27**, 955 (2009).
23. S. Irusta, L. M. Cornaglia and E. A. Lombardo, *Mater. Chem. Phys.*, **86**, 440 (2004).
24. R. P. Turcotte, J. O. Sawyer and L. Eyring, *Inorg. Chem.*, **8**, 238 (1969).
25. T. Levan, M. Che, J. M. Tatibouet and M. Kermarec, *J. Catal.*, **142**, 18 (1993).
26. J. Ni, L. Chen, J. Lin, M. K. Schreyer, Z. Wang and S. Kawi, *Int. J. Hydrog. Energy*, **38**, 13631 (2013).

Supporting Information

Structural properties of disordered macroporous $La_2O_2CO_3$/ZnO materials prepared by a solution combustion method

Hongyan Yu*,, Yong Men**, and Eun Woo Shin*,†**

*School of Chemical Engineering, University of Ulsan Daehakro 93, Nam-gu, Ulsan 44610, Korea
**College of Chemistry and Chemical Engineering, Shanghai University of Engineering Science, No. 333 Longteng Road, Songjiang District, Shanghai 201620, P. R. China
(*Received 23 November 2018 • accepted 30 January 2019*)

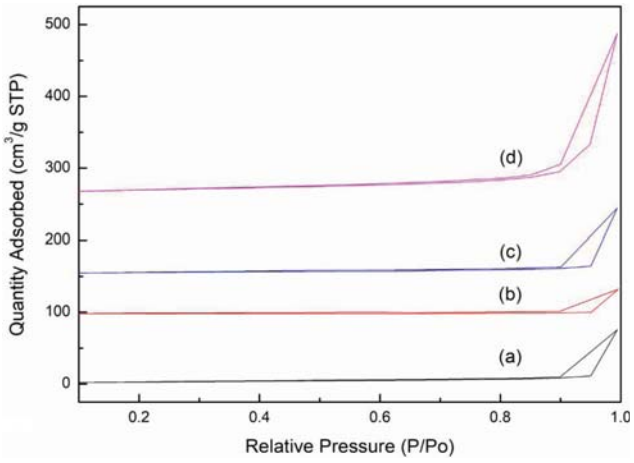

Fig. S1. Nitrogen adsorption-desorption isotherm of (a) CoLZ-0.125-500, (b) CoLZ-0.25-500, (c) CoLZ-1-500 and (d) CoLZ-2-500.

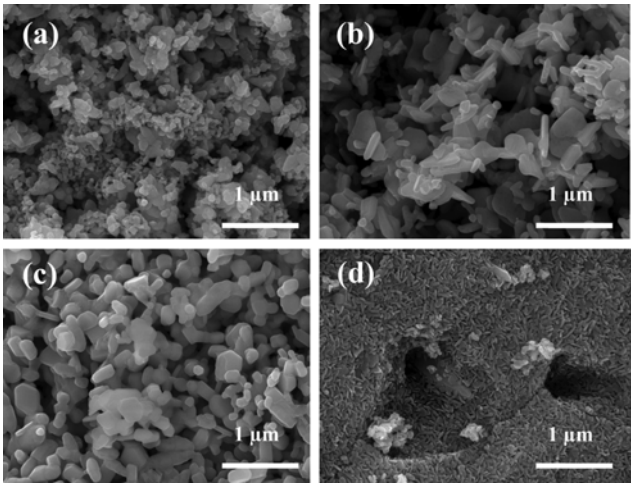

Fig. S2. FE-SEM images of (a) CoLZ-0.125-500, (b) CoLZ-0.25-500, (c) CoLZ-1-500 and (d) CoLZ-2-500.

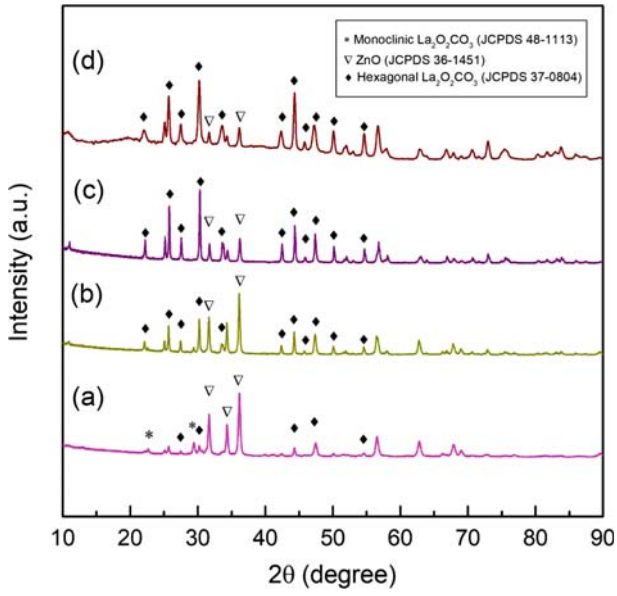

Fig. S3. XRD patterns of (a) CoLZ-0.125-500, (b) CoLZ-0.25-500, (c) CoLZ-1-500 and (d) CoLZ-2-500.

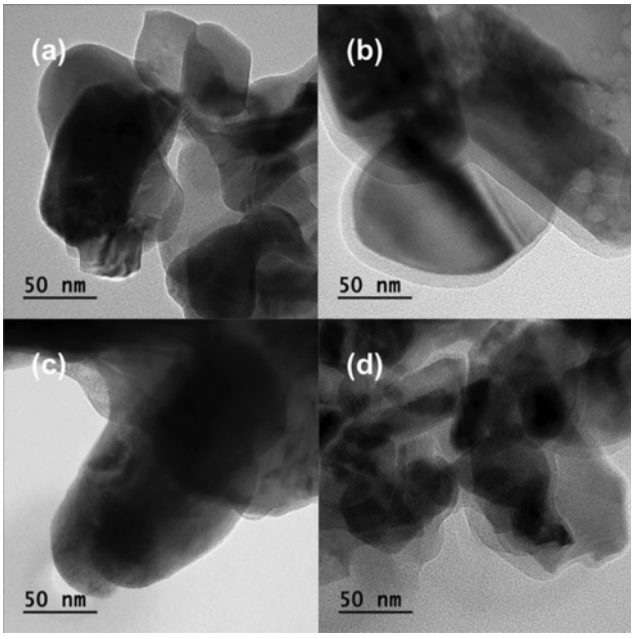

Fig. S4. FE-TEM images of (a) CoLZ-0.125-500, (b) CoLZ-0.25-500, (c) CoLZ-1-500 and (d) CoLZ-2-500.

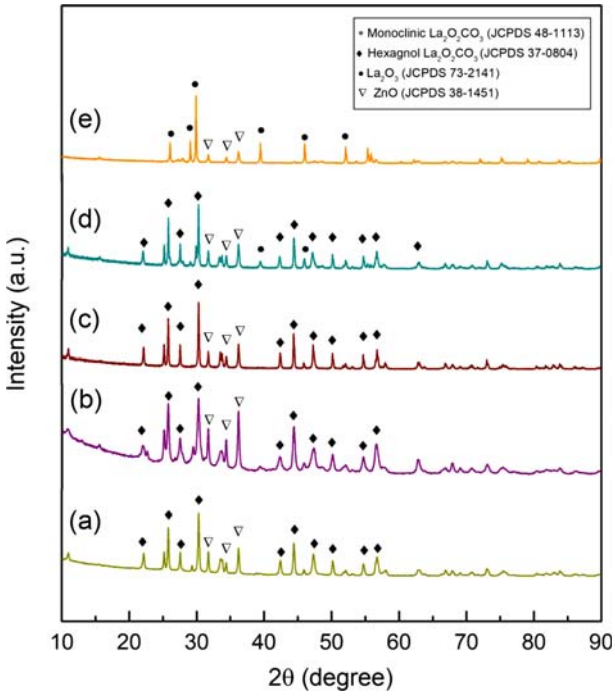

Fig. S5. XRD patterns of LZ-1 materials calcined at different temperatures (a) CoLZ-1-500, (b) CoLZ-1- 550, (c) CoLZ-1-600, (d) CoLZ-1-650and (e) CoLZ-1-700.